THE EFFECT OF MECHANICAL PROPERTIES ON POLYMER DEFORMATION AND FLOW SUSPENSION IN THE SELECTIVE LASER SINTERING PROCESS

Rihabe BELGADA[*] and Khalid ZARBANE
(LARILE) Laboratory of Advanced Research on Industrial and Logistics Engineering, ENSEM,
Hassan II University of Casablanca, MOROCCO
E-mail: belgada.rihab@gmail.com

Ahmed MZERD
(SSTE) Faculty of Science, Mohammed V University, Department of Physic,
Mechanical Engineering, Rabat, MOROCCO

Among the various additive manufacturing processes, there is selective laser sintering, with the use of a high-power laser that sinters the small particles of polymer powder and turn them into a solid structure, from a 3D model, nowadays SLS additive manufacturing has become the best choice for the industry, especially for polymer materials, SLS ensures high productivity and well-honed materials at low cost. Recent advances in fitting, the materials and software have made SLS printing accessible to a wider range of activities. Our study is to show the mechanism of polymer particle suspension during the three stages of selective laser sintering printing, we start with printing first, the polymer powder in a thin layer applied on a flat shape inside the build chamber and the printer will heat the powder until the polymer melts, Allowing the laser to easily increase the temperature in specific areas in the powder bed to trace the morphology of the solidified part. Secondly, cooling and finally post-processing to extract the finished parts from the build chamber. In our study, we will analyze the suspension of small polymer powder particles in the SLS printing process. We will start with the mathematical formulation of the problem with an experimental study of the polymer sample studied. Next, we will set up the chosen solution method and finally the modeling of the results obtained on the FORTRAN language.

Key words: additive manufacturing, small polymer, selective laser sintering, suspension of polymer granule, flow deformation.

1. Introduction

Selective laser sintering is a laser additive manufacturing process that consists of manufacturing parts from a 3D model by sintering small powdered polymer particles to fuse them together. Among these advantages are the flexibility of production, the geometry can be changed during production and also the manufacture of robust parts. In this study, we are mainly interested in the polymer powder bed to model the phenomenon of suspension and flow deformation of these small polymer particles during the additive manufacturing process by selective laser sintering. We have treated this phenomenon by using a polypropylene-type polymer powder, because it is semi-rigid and contains a high resistance to fatigue and bending, tear-resistant and chemically inert. The innovation and invention that drives our study is usually evident in the morphology of polypropylene seeds as well as its suspension during fusion treatment by the selective laser fusion additive manufacturing process. [14], [18], [19].
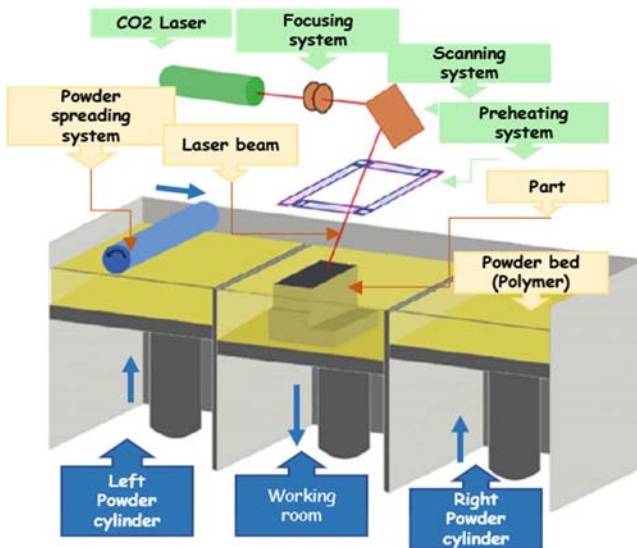
---

[*] To whom correspondence should be addressed

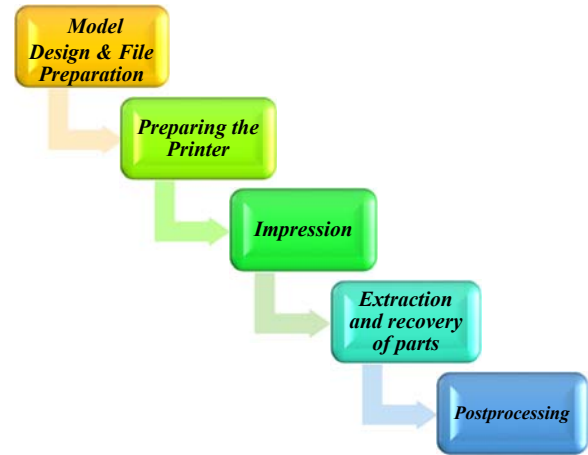Fig.1. Simplified diagram of the SLS manufacturing process of polymer.

Fig.2. Selective laser sintering additive manufacturing process SLS.

2. Mathematical modeling

2.1. Continuity equation

The continuity equation in the case of incompressible flows then reduces to:

$$div\left(\vec{U}\right) = 0 \,, \tag{2.1}$$

where $\vec{U} = \alpha \vec{e_x} + \beta \vec{e_z}$ is the fluid velocity.

2.2. Transport equation

The concentration of polymer granules within an airflow obeys the following transport equation:

$$\frac{\partial C_g}{\partial t} + \left(\vec{U}\vec{\nabla}C_g\right) = M_m \, \psi C_g \,. \tag{2.2}$$

2.3. Quantity of motion equation

The Navier-Stokes momentum conservation equation:

$$\vec{I_v}(t) = m_v(t)\vec{v} = \int_v \rho\vec{v}\,dv \,, \tag{2.3}$$

$$\frac{D\vec{I_v}}{Dt} = \lim_{\Delta t \to 0} \frac{\vec{I_v}(t+\Delta t) - \vec{I_v}(t)}{\Delta t} \,, \ \vec{I_v}(t+\Delta t) = \vec{I_v}(t+\Delta t) + \left(\vec{I_2} - \vec{I_1}\right) \,,$$

$$\left(\vec{I_2}-\vec{I_1}\right)=\int_s\left(\rho\vec{v}\vec{n}\right)\vec{v}\,\Delta t\,ds \,,\; \frac{D\vec{I_v}}{Dt}=\frac{\partial\vec{I_v}}{\partial t}+\int_s\left(\rho\vec{v}\vec{n}\right)\vec{v}\,ds=\sum\vec{F}\,.$$

With : $\sum\vec{F}=\vec{F_m}+\vec{F_s}$

$$\vec{F_m}=\int_s\rho\vec{f}\,dv \,,\; \vec{F_s}=\int_s p\vec{n}\,ds \,,\tag{2.4}$$

$$\int_v\frac{\partial}{\partial t}\left(\rho\vec{v}\right)dv+\int_s\left(\rho\vec{v}\vec{n}\right)\vec{v}\,ds=\int_v\rho\vec{f}\,dv+\int_s p\,ds\,\vec{n}\,,\tag{2.5}$$

$$\int\frac{\partial\vec{v}}{\partial t}+\rho\left(\vec{v}\nabla\right)\vec{v}=-\overrightarrow{div}(p)+\rho\vec{f}+\overrightarrow{div}(\sigma)\,.\tag{2.6}$$

3. Experimental study

3.1. Scanning electron microscope

We did an analysis for the sample studied on the scanning electron microscope and an energy dispersive X-ray spectroscopy in our laboratory to find out the morphology as well as the chemical properties of the sample.
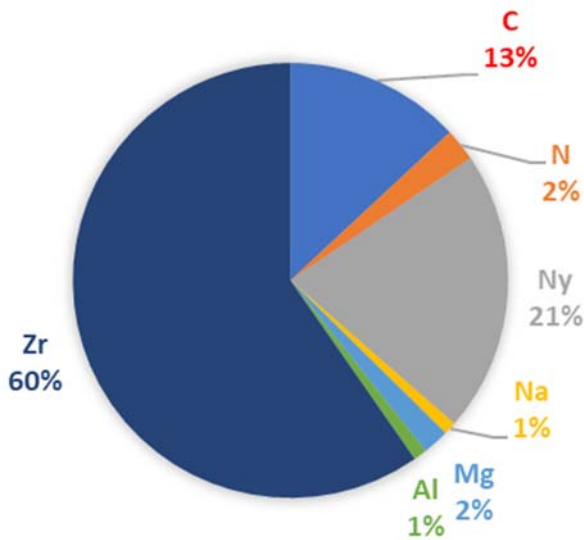
Fig.3. The mass of the chemical components of polypropylene by energy-dispersive X-ray spectroscopy EDXS
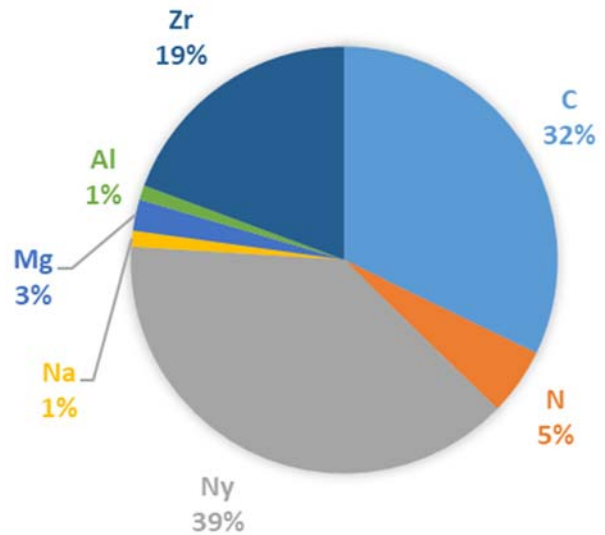
Fig.4. Atomic composition of the chemical components of Polypropylene by energy-dispersive X-ray spectroscopy EDXS

Figures 3 and 4 show the mass and atomic composition of the sample studied by energy dispersive X-ray spectroscopy EDXS.
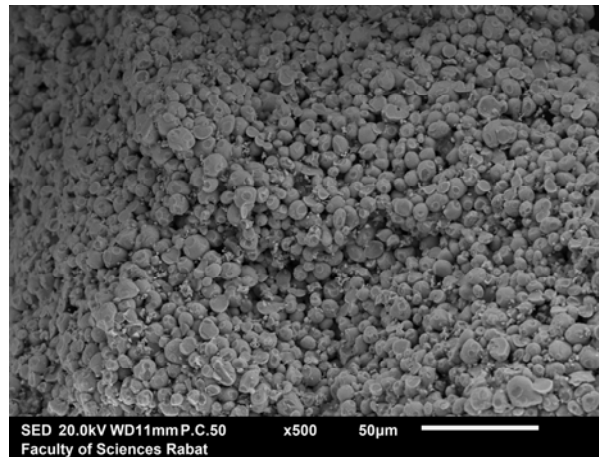
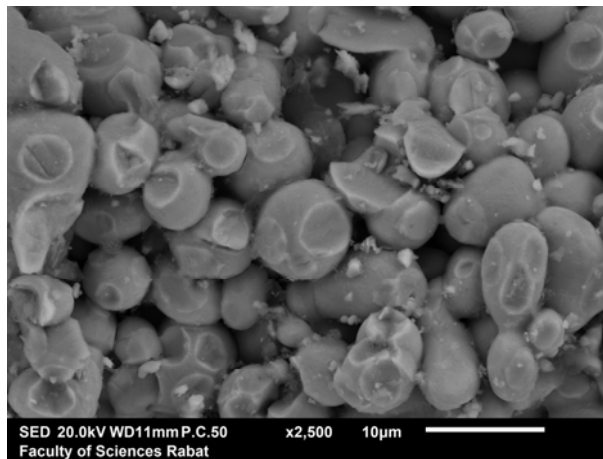Fig.5. Polypropylene granule in scanning electron microscope (SEM)×100.

Fig.6. Polypropylene granule in scanning electron microscope (SEM)×500.
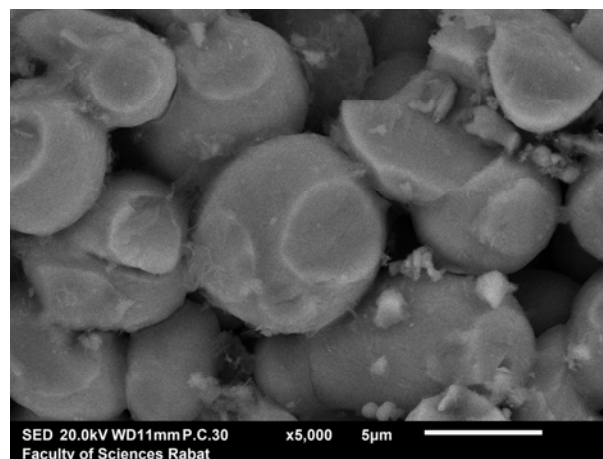

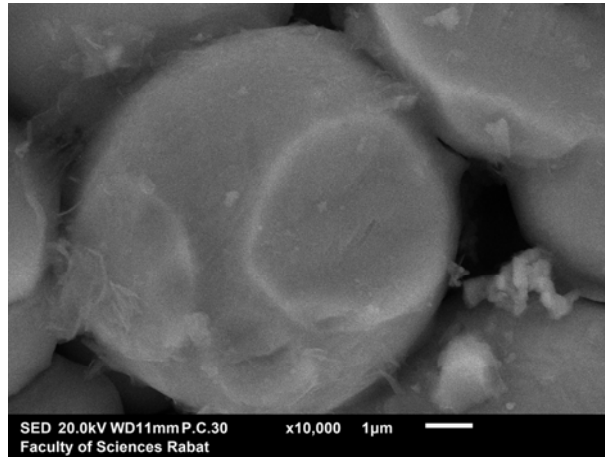Fig.7. Polypropylene granule in scanning electron microscope (SEM)×1000.

Fig.8. Polypropylene granule in scanning electron microscope (SEM)×10000.

Figures 5, 6, 7 and 8 show the geometric morphology of polypropylene granules and the texture and shape of the granules on scanning electron microscopy (SEM).

3.2. Effective thermal conductivity of powder

Numerous numerical and experimental methods have been developed to determine the thermal conductivity of granular media. For example, there is the plate method (ISO 8302) (3). It is a stationary measurement method used for Solid materials with low thermal conductivity for which the contact resistances in relation to the strength of the material. The experiment consists of two outer plates, made of a highly conductive material, at a constant temperature by circulation of a fluid and a third heating plate in the middle which transmits uniform heating power through the sample to be measured thermal conductivity [9], [10], [11], [12], [14].

A simplified model was first developed using the FLUENT software. In this model a column of Polymer powder *40 mm* in diameter and *200 mm* in height is considered with an effective thermal conductivity of *0.4 W / (mK)*. A curve of the evolution of the temperature was calculated throughout the height of the column (Fig.9) [13], [15].
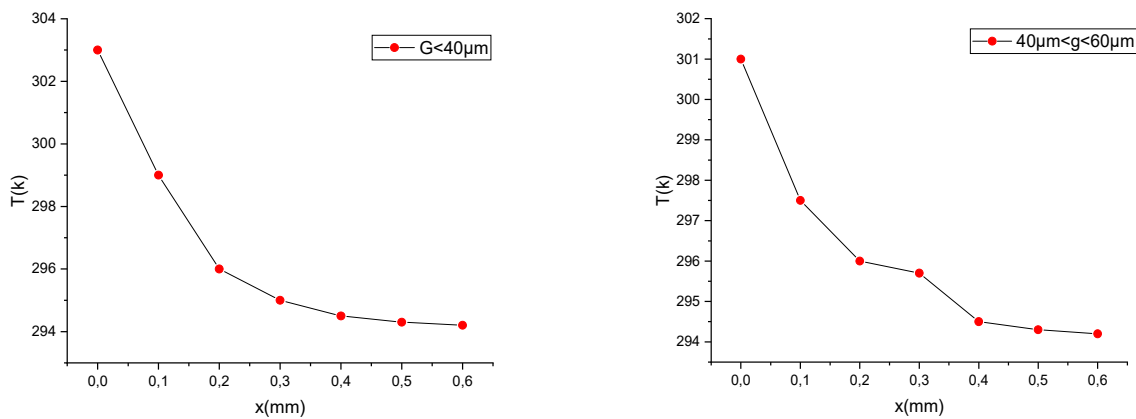

Fig.9. Axial temperature profiles for different powder particle sizes.
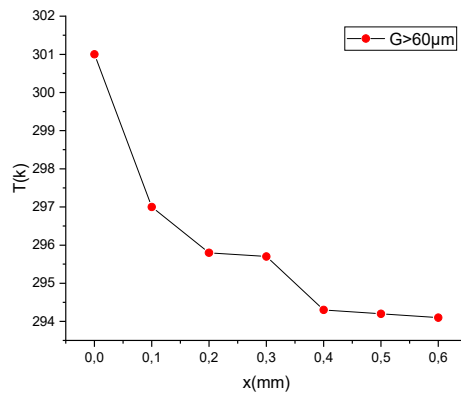
Fig.9 cont. Axial temperature profiles for different powder particle sizes.

3.3. Polymer particle dimension

The histograms show that the dominant dimensions of the polymer particles obtained for *0.4*, *0.8* and *1.2 m/s*. One found that a scan rate of *1.2 m/s* provides more particle dominance small sizes. The images in Fig.10 show that there are occasional particles as large in diameter as *40 μm* [4], [5], [6], [16].
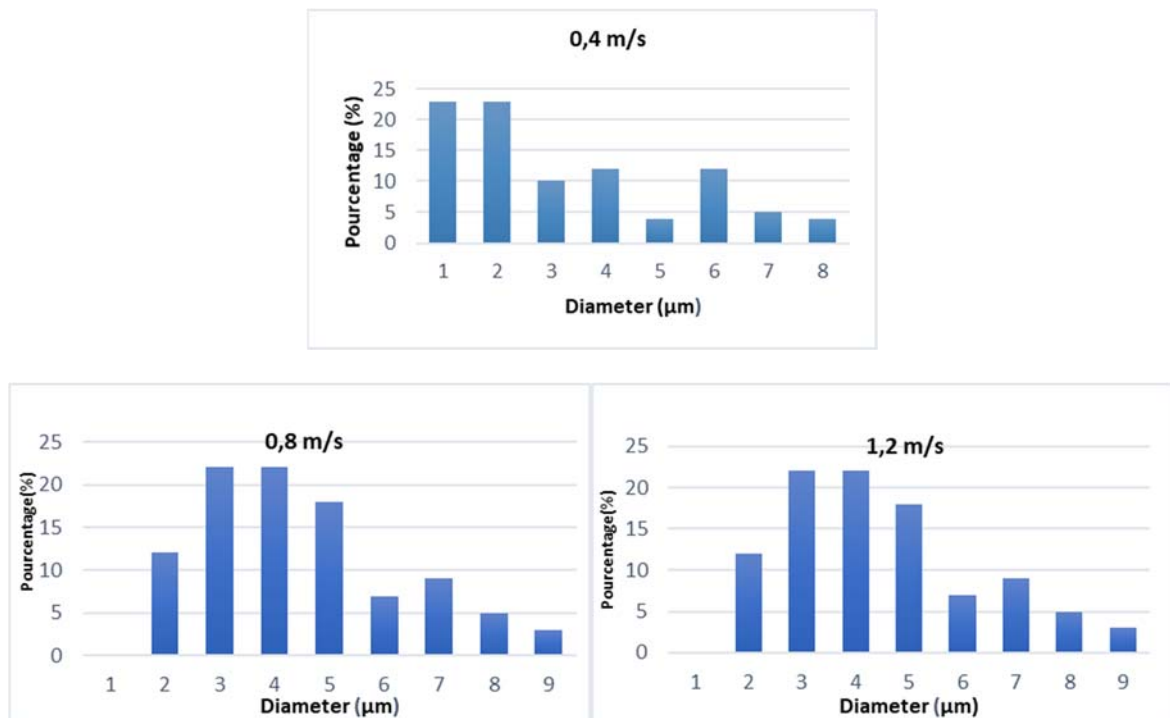

Fig.10. Histograms of polymer particle size distribution deposited on the slides of glass at a height of *2 mm* with *200 W* laser power and scan speeds different.

This step experimentally highlighted the phenomena generated during the SLS process. The experiments carried out and described during this stage have made it possible to determine the data necessary for the implementation of a numerical model which will be the subject of the next stage.

It has been shown that the interaction of the laser beam with the powder bed leads not only to the melting of the polymer but also to the formation of a vapor above the melt pool and the ejection of molten polymer droplets [7], [8].

4. Method of resolution

4.1. Meshing

Each point in the physical domain that stores a scalar or vector quantity satisfies the differential equations of the mathematical model, governing our physical phenomenon. To project these equations onto this domain, we subdivide it into a number of finite volumes, localized by means of indices *i* and *j*, in each middle of each volume we consider *G* points, called control volume centers *E*, *O*, *N*, and *S* are the centers of the volumes to the east, west, north and south of the *G* center. The faces of a typical control volume are located at points *e*, *o*, *n*, and *s*. Each control volume has a dimension Δx, Δy and *l*. In the center of each control volume the scalar variables (*p* and *o*) are stored, but for the vector quantities (the speeds and), they are located on the faces of the control volume (Figs 11 and 12).
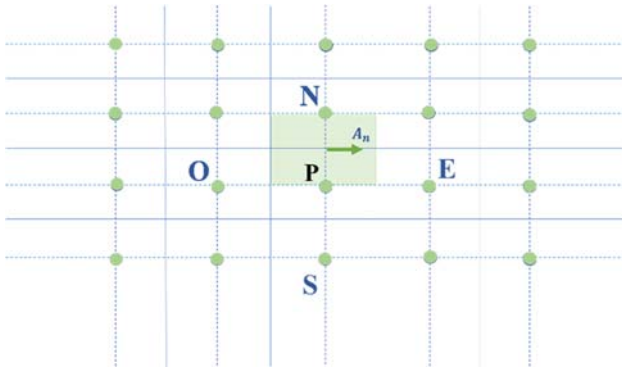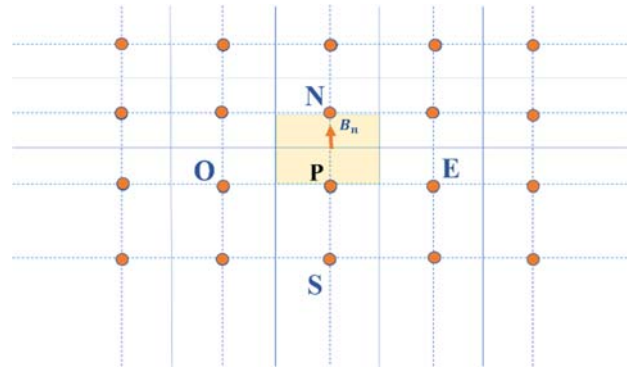

Fig.11. Control volume shifted upwards.   Fig.12. Control volume shifted to the right.

G is the principal node, *i* is the discretization index along the *x*-axis, and *j* is the discretization index of discretization along the "*z*" axis. In general, the letters *E*, *O*, *N*, and *S* represent East, West, North, and South, respectively. The square represents a control volume element. The segments [*GE*] and [*GN*] are Δx and Δz, respectively.

4.2. Discretization of equations

4.2.1. Discretization of continuity equation

$$\int_{t}^{t+\Delta t}\int_{o}^{e}\frac{\partial A}{\partial x}\,dv\,dt + \int_{t}^{t+\Delta t}\int_{o}^{n}\frac{\partial B}{\partial z}\,dv\,dt = 0 \,. \tag{4.1}$$

With: $dv = dx\,dz\,l$,

$$\int_{t}^{t+\Delta t}\Delta z\left(A_{e}-A_{o}\right)dt + \int_{t}^{t+\Delta t}\Delta x\left(B_{n}-B_{s}\right)dt = 0 \,, \tag{4.2}$$

$$\int\limits_{t}^{t+\Delta t} \Delta z\big(A(i+1,j)-A(i,j)\big)dt + \int\limits_{t}^{t+\Delta t} \Delta x\big(B(i,j+1)-B(i,j)\big)dt = 0\,, \tag{4.3}$$

$$\Delta z\Big[A^{t+\Delta t}(i+1,j)-A^{t+\Delta t}(i,j)\Big] + \Delta x\Big[B^{t+\Delta t}(i,j+1)-B^{t+\Delta t}(i,j)\Big] = 0\,. \tag{4.4}$$

4.2.2. Discretization of quantity of motion equation

- Speed A:

$$\int\limits_{t}^{t+\Delta t}\int\limits_{V_A}\frac{\partial A}{\partial t}dv\,dt + \int\limits_{t}^{t+\Delta t}\int\limits_{o}^{e}\frac{\partial(AA)}{\partial x}dv\,dt + \int\limits_{t}^{t+\Delta t}\int\limits_{s}^{n}\frac{\partial(AB)}{\partial x}dv\,dt = -\int\limits_{t}^{t+\Delta t}\int\limits_{o}^{e}\frac{\partial P}{\partial x}dv\,dt\,. \tag{4.5}$$

$$a_{P_A}A^{t+\Delta t}(i,j)+a_{E_A}A^{t+\Delta t}(i+1,j)+a_{O_A}A^{t+\Delta t}(i-1,j)+$$
$$+a_{N_A}A^{t+\Delta t}(i,j+1)+a_{S_A}A^{t+\Delta t}(i,j-1)=R_A. \tag{4.6}$$

$$a_{P_A}=\frac{\Delta x\Delta z}{\Delta t}+\frac{\Delta z}{2}\Big[A_e^{t+\Delta t}-A_o^{t+\Delta t}\Big]+\frac{\Delta x}{2}\Big[B_n^{t+\Delta t}-B_s^{t+\Delta t}\Big], \tag{4.7}$$

$$a_{E_A}=\frac{\Delta z}{4}\Big[A^{t+\Delta t}(i+1,j)+A^{t+\Delta t}(i,j)\Big],\ a_{O_A}=-\frac{\Delta x}{4}\Big[A^{t+\Delta t}(i,j)+A^{t+\Delta t}(i-1,j)\Big], \tag{4.8}$$

$$a_{N_A}=\frac{\Delta x}{2}\Big(B_n^{\ t+\Delta t}\Big),\ \ a_{S_A}=-\frac{\Delta x}{2}\Big(B_s^{\ t+\Delta t}\Big),$$

$$\tag{4.9}$$

$$R_A=\frac{\Delta x\Delta z}{\Delta t}A^t(i,j)+\Delta z\Big[P^{t+\Delta t}(i-1,j)-P^{t+\Delta t}(i,j)\Big].$$

- Speed B:

$$\int\limits_{t}^{t+\Delta t}\int\limits_{V_B}\frac{\partial B}{\partial t}dv\,dt + \int\limits_{t}^{t+\Delta t}\int\limits_{o}^{e}\frac{\partial(BA)}{\partial x}dv\,dt + \int\limits_{t}^{t+\Delta t}\int\limits_{s}^{n}\frac{\partial(BB)}{\partial z}dv\,dt = -\int\limits_{t}^{t+\Delta t}\int\limits_{s}^{n}\frac{\partial P}{\partial z}dv\,dt + \varphi\int\limits_{t}^{t+\Delta t}\int\limits_{s}^{n}dv\,dt\,. \tag{4.10}$$

With $\varphi=\dfrac{gL}{\vartheta^2}$,

$$a_{P_B}B^{t+\Delta t}(i,j)+a_{E_B}B^{t+\Delta t}(i+1,j)+a_{O_B}B^{t+\Delta t}(i-1,j)+$$
$$+a_{N_B}B^{t+\Delta t}(i,j+1)+a_{S_B}B^{t+\Delta t}(i,j-1)=R_B, \tag{4.11}$$

$$a_{P_B}=\frac{\Delta x\Delta z}{\Delta t}+\frac{\Delta z}{2}\Big[A_e^{t+\Delta t}-A_o^{t+\Delta t}\Big]+\frac{\Delta x}{4}\Big[B_n^{t+\Delta t}(i,j+1)-B_s^{t+\Delta t}(i,j-1)\Big], \tag{4.12}$$

$$a_{E_B}=\frac{\Delta z}{2}\Big(A_e^{\ t+\Delta t}\Big),\ a_{O_B}=-\frac{\Delta z}{2}\Big(A_o^{\ t+\Delta t}\Big), \tag{4.13}$$

$$a_{N_B} = \frac{\Delta x}{4}\left[B^{t+\Delta t}(i,j) + B^{t+\Delta t}(i,j+1)\right], \ a_{S_B} = -\frac{\Delta x}{4}\left[B^{t+\Delta t}(i,j) + B^{t+\Delta t}(i,j-1)\right], \quad (4.14)$$

$$R_B = \frac{\Delta x \Delta z}{\Delta t}B^t(i,j) + \Delta x \Delta z \varphi + \Delta x\left[P^{t+\Delta t}(i,j-1) - P^{t+\Delta t}(i,j)\right]. \quad (4.15)$$

4.2.3. Discretization of transport equation

$$\int_{t}^{t+\Delta t}\int_{V_{C_p}}\frac{\partial C_p}{\partial t}dvdt + \int_{t}^{t+\Delta t}\int_{o}^{e}\frac{\partial(C_p A)}{\partial x}dvdt + \int_{t}^{t+\Delta t}\int_{s}^{n}\frac{\partial(C_p B)}{\partial z}dvdt =$$

$$= \psi\int_{t}^{t+\Delta t}\int_{o}^{e}\frac{\partial}{\partial x}\left(\frac{\partial C_p}{\partial x}\right)dvdt + \psi\int_{t}^{t+\Delta t}\int_{s}^{n}\frac{\partial}{\partial z}\left(\frac{\partial C_p}{\partial z}\right)dvdt. \quad (4.16)$$

With $\psi = \dfrac{\phi_p}{L\vartheta_0}$,

$$a_{P_{C_p}}C_p^{t+\Delta t}(i,j) + a_{E_{C_p}}C_p^{t+\Delta t}(i+1,j) + a_{O_{C_p}}C_p^{t+\Delta t}(i-1,j) +$$

$$+ a_{N_{C_p}}C_p^{t+\Delta t}(i,j+1) + a_{S_{C_p}}C_p^{t+\Delta t}(i,j-1) = R_{C_p}, \quad (4.17)$$

$$a_{P_{C_p}} = \frac{\Delta x \Delta z}{\Delta t} + \frac{\Delta z}{2}\left[\begin{matrix}A^{t+\Delta t}(i+1,j)\\-A^{t+\Delta t}(i,j)\end{matrix}\right] + \frac{\Delta x}{2}\left[\begin{matrix}B^{t+\Delta t}(i,j+1)\\-B^{t+\Delta t}(i,j-1)\end{matrix}\right] + 2\psi\left(\frac{\Delta z}{\Delta x} - \frac{\Delta x}{\Delta z}\right), \quad (4.18)$$

$$a_{E_{C_p}} = \frac{\Delta z}{2}A^{t+\Delta t}(i+1,j) - \psi\frac{\Delta z}{\Delta x}, \ a_{O_{C_p}} = -\frac{\Delta z}{2}A^{t+\Delta t}(i,j) - \psi\frac{\Delta z}{\Delta x}, \quad (4.19)$$

$$a_{N_{C_p}} = \frac{\Delta x}{2}B^{t+\Delta t}(i,j+1) - \psi\frac{\Delta x}{\Delta z}, \quad (4.20)$$

$$a_{S_{C_p}} = -\frac{\Delta x}{2}B^{t+\Delta t}(i,j) - \psi\frac{\Delta x}{\Delta z}, \quad (4.21)$$

$$R_{C_p} = \frac{\Delta x \Delta z}{\Delta t}C_p^t(i,j). \quad (4.22)$$

5. Results and discussions

A spectrometric study has shown that this plume does not contain ionized species but only certain excited species of the material studied. The phenomenon of absorption of laser light by this plume has been discarded and it has been shown to remain neutral with respect to the passage from the laser beam to the target. After presenting all the conceptual, mathematical and numerical bases in. the objective of this study phase is to present the results obtained by the code established in FORTRANT. Calculations are initiated by an initial profile, which can be absolutely nondescript as long as it meets boundary conditions. However, to reduce the computation time, an initial profile was used that was closer to the actual profile chosen. Then, a profile that corresponds to a flow of a Newtonian fluid continuous in a flat tube is adopted.
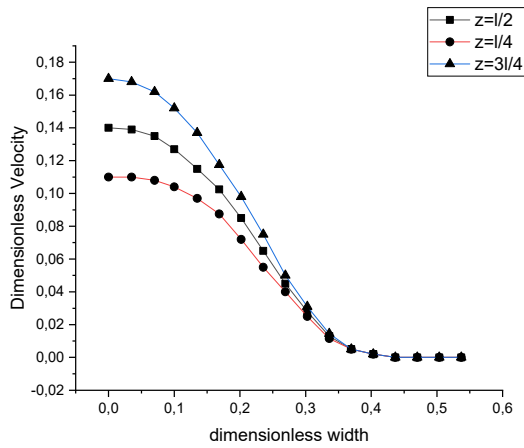
Fig.13. Profile of *3* dimensionless axial velocity.
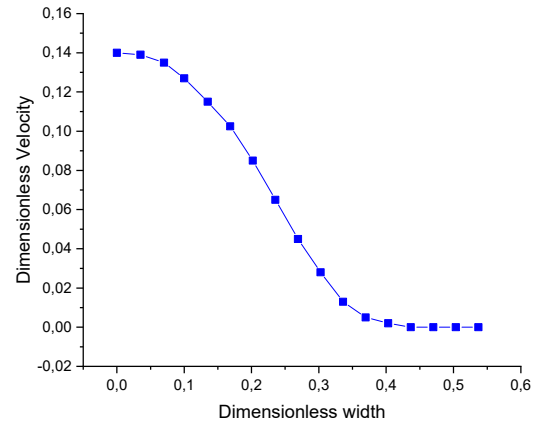

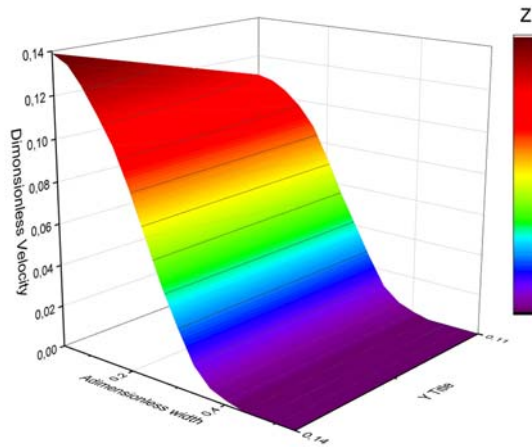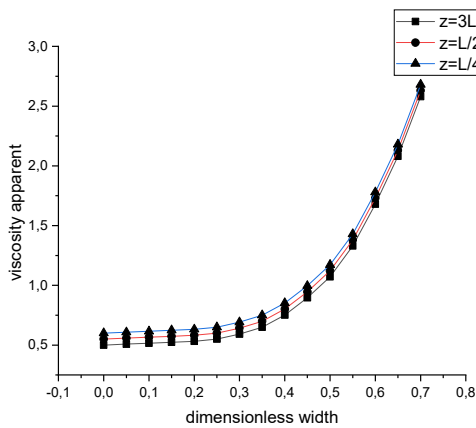Fig.14. Profile of dimensionless axial velocity.

Fig.15. 3D Surface of dimensionless axial velocity.

Figures 13, 14 and 15 show the profile of the axial velocity as a function of the radius. It can be said that as the polymer approaches the duct wall, the axial velocity decreases, when the polymer reaches the outlet of the tube, the axial velocity increases. This can be because the polymer becomes in a molten state and the particles become disorganized and slide between them more easily [1], [17], [19].

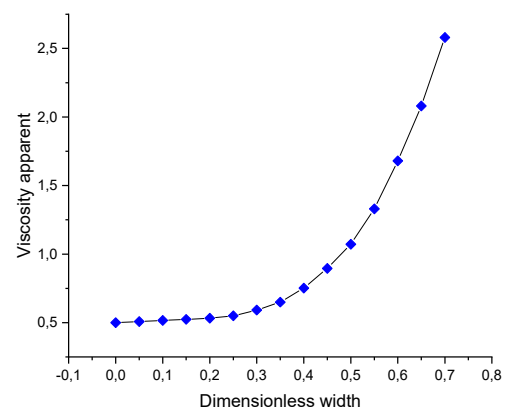Fig.16. Profile of *3* dimensionless apparent velocity.

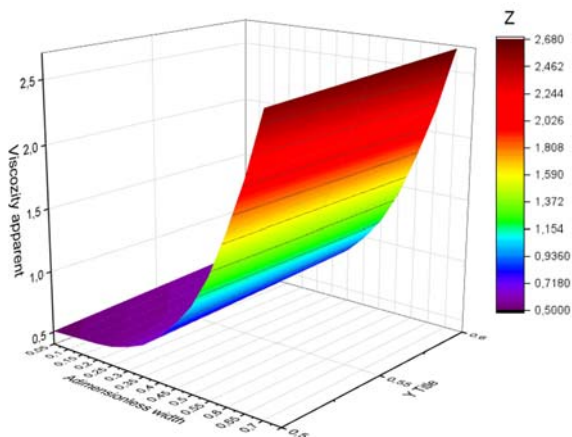Fig.17. Profile of dimensionless apparent velocity.

Fig.18. Surface of 3D dimensionless apparent velocity.

Figures 16, 17 and 18 show the profile of the apparent viscosity with respect to the three-section radius of the tube. It can be noticed that, the polymer becomes melted with a very high temperature, which causes a low number of three-dimensional nodes in the bonding network, per unit volume of polymer, resulting in a decrease in the viscosity of the polymer [1], [3], [18].
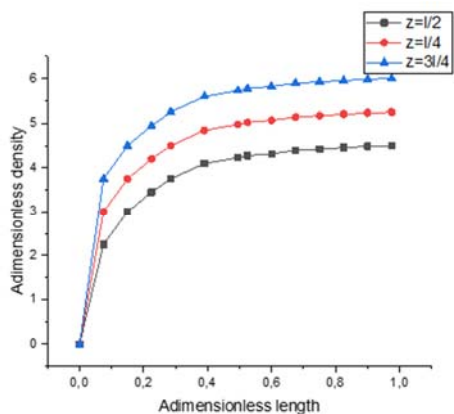

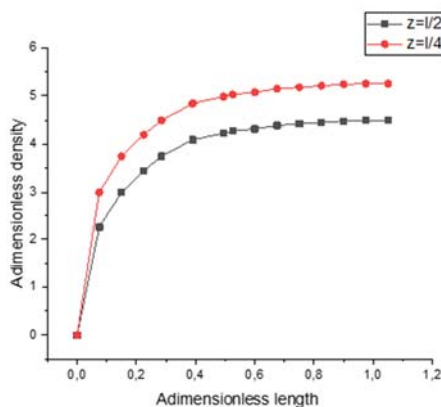Fig.19. Profile of 3 dimensionless density.

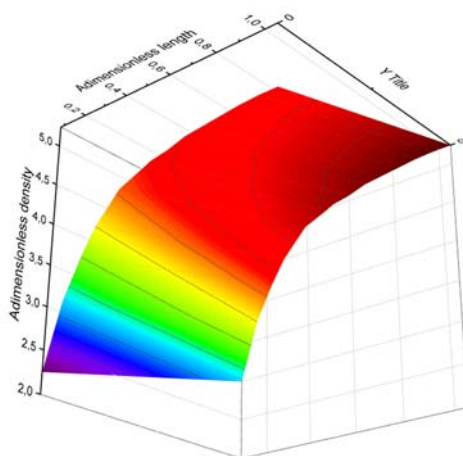Fig.20. Profile of two dimensionless density.

Fig.21. 3D Surface of dimensionless density.

Figures 19, 20 and 21 show the profile of the density. From this curve, we can see that the density near the wall is approaching unity. The result obtained can be explained by the fact that the molten polymer is considered to be an incompressible fluid in some parts of the tube wall [3], [18], [19].
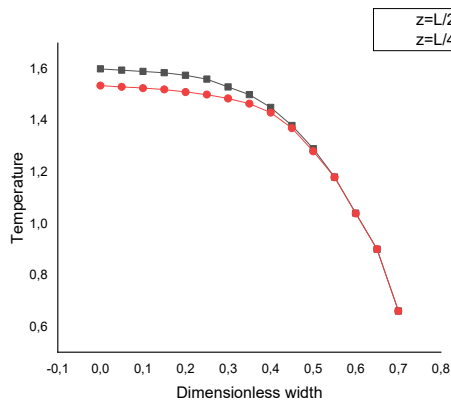

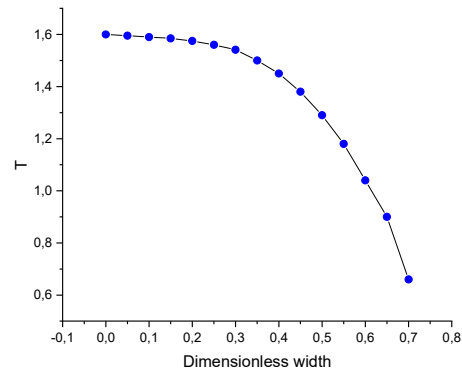Fig.22. Profile of two dimensionless temperature.
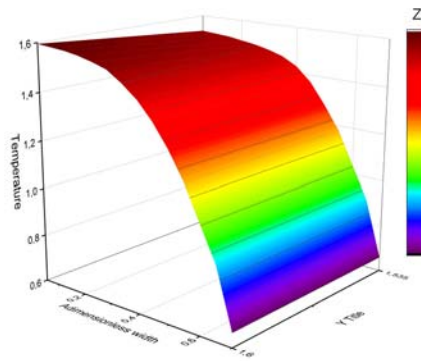

Fig.23. Profile of dimensionless temperature.

Fig.24. 3D surface of dimensionless temperature

Figures 22, 23 and 24 illustrate the dimensionless temperature profile in two different sections of the pipe. We can see that the axial velocity increases the time that the polymer changes the state from solid to liquid, and thanks to this increase we obtain a small separation of the constituent molecules, which causes an increase in temperature. More than the temperature range increases. We can also see that the polymer is getting closer to the outlet of the tube. [1], [18], [19].
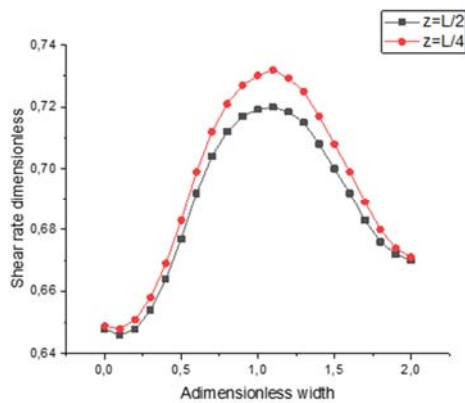

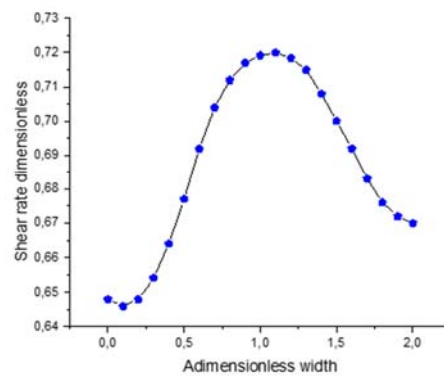
Fig.25. Profile of two dimensionless shear rate.

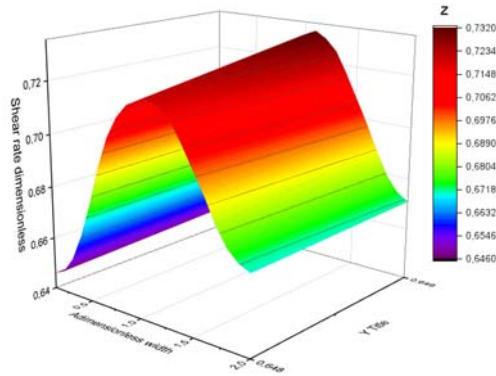Fig.26. Profile of dimensionless rate shear.

Fig.27. 3D Surface of dimensionless rate shear.

Figures 25, 26 and 27 show the shear rate profile in different sections of the pipe. It can be seen that the shear rate increases as the radius increases. and that the shear rate decreases as the radius continues to increase. It can also be seen that when the section is close to the exit of the tube, the shear rate is high.
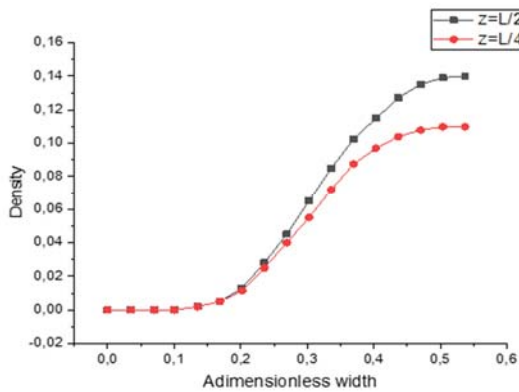

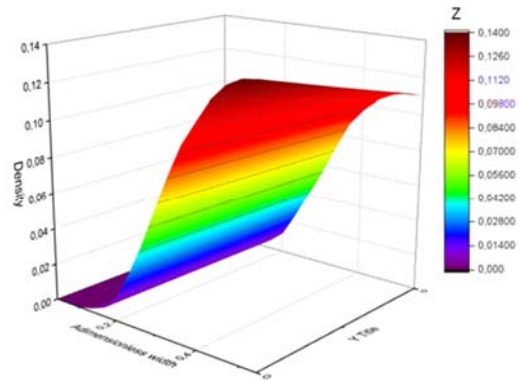Fig.28. Profile of two dimensionless density.   Fig.29. 3D Surface of two dimensionless density.

Figures 28 and 29 illustrate the profile of the volume density as a function of time., we can see that the volume density is close to the unit near the wall. This effect can be interpreted as the molten polymer can be considered as an incompressible fluid in certain areas near the tube wall [2], [3], [28], [29].

6. Conclusion

We made a numerical model reproducing the main characteristics to see the deformation and flow suspension of the polymer in the SLS process. The heat source produced by the laser travels over a bed of powder spread over a substrate. The substrate consists of the polymer powder layers that have already been fused and consolidated. The operation takes place in a protective gas environment whose pressure can be controlled. The model also allows the consideration of the thermophysical properties of the material that depend on the temperature and, therefore, it allows the consideration of changes in the physical state of the material during the SLS process. The results obtained show that the effect of mechanical properties on polymer deformation and flow suspension in the selective laser sintering process plays a very important role, especially for speed, density and temperature.

Acknowledgements

Nomenclature

C_g – granule concentration

α, β – velocity components

δ_c – number of Schmidt

κ_r – rate of dissipation of the turbulent kinetic energy

κ_t – energy kinetic turbulent

μ_M – dynamic viscosity

υ_f – viscosity of fluid kinematic

ϕ_g – granule diameter

Ψ – step at the moment t in space

References

[1] Gotoh K., Morooka H. and Nishimura T. (2001): *Effect of number density of deposited particles on resuspension fraction from sparse particle bed.*– J. Aerosol Sci., vol.32, No.1, pp.559-560.

[2] Gueraoui K., Taibi M., Ghouli A., Mrabti A., Zeggwagh G. and Haddad Y. (2008): *Pulsating flow of inelastic fluids in anisotropic porous viscoelastic tubes.*– International Review of Mechanical Engineering, vol.2, No.3, pp.506-512.

[3] Phillips M. (1980): *A force balance model for particle entrainment into a fluid stream.*– J. Phys. D, Appl. Phys., vol.13, No.2, pp.221.

[4] Chávez-Negrete C., Domínguez-Mota F.J. and Santana-Quinteros D. (2018): *Numerical solution of Richards' equation of water flow by generalized finite differences.*– Computers and Geotechnics, vol.101, pp.168-175.

[5] Ramar M. and Lakshmanan M. (2023): *Mechanical and tribological properties of SS316L with comparison of SLM and casting methods.*– Materials Today Proceeding, DOI:10.1016/j.matpr.2023.03.333.

[6] Echchikhi A., Gueraoui K., El Houssaine El Rhaleb, Kifani-Sahban F., Benbih H. and Bounouar A. (2020): *Thermal treatments of wood (eucalyptus and maritime pin).*– Experimental and Theoretical Study with Chemical Characterization, vol.8, No.6. (IREA), pp.223.

[7] Zakham N., Ammari A., El Rhaffari Y., Cherraj M., Bouabid H., Gueraoui K. and Samaouali A. (2020): *The effect of cement content on the thermo-mechanical performance of compressed earth block.*– International Review of Civil Engineering (IRECE), vol.11, No.6, pp. 249-256.

[8] Samrani H., Gueraoui K., Zeggwagh N.A. and Taibi M. (2021): *Modeling of the impact of the geometric shape of a solar dryer on heat energy for different region in Morocco.*– vol.9, No2. (IREA), pp.104-114.

[9] Maftouh A., El Fatni O., Echchikhi A., Bahaj T., Gueraoui K. and El Houssaine El Rhaleb (2022): *Effect of feed water temperature on reverse osmosis performance in a borehole water desalination plant.*– Numerical and Experimental Validation, vol.10, No.4. (IREA), pp.252.

[10] El Hamma M., Rtibi A., Taibi M., Gueraoui K. and Bernatchou M. (2023): *Theoretical and numerical study of thermosolutal convection in a cylindrical porous cavity filled with a nanofluid and taking into account Soret and Dufour effects.*– vol.10, No.1, (IREA), pp.197-206.

[11] Dirisu G.B., Okonkwo U.C., Okokpujie I.P. and Fayomi O.S. (2018): *Comparative analysis of the effectiveness of reverse osmosis and ultraviolet radiation of water treatment.*– Journal of Ecological Engineering, vol.20, No.1, pp.61-75.

[12] Nchiti E., El Hammoumi A., Gueraoui K. and Iben Brahim A.(2020): *A comparative study of seismic and tsunami vulnerability of structures located in the coastal area of Rabat-Salé, Morocco.*– (IREME), vol.14, No.4, p.264.

[13] Belgada R., Gueraoui K., Mzerd A., Bellahkim M., Benbih H. (2020): *A biological degradation model of sunflower waste with comparison of the growth profiles of microorganisms between the meal and the complete sunflower seed.*– (IREA), vol.8, No.3, p.107.

[14] Šuba R. (2022): *Sustainability aspects of parts additive manufacturing from metal powder.*– Res. Pap. Fac. Mater. Sci. Technol. Slovak Univ. Technol., vol.30, No.55, pp.37-44.

[15] Belgada R., Gueraoui K., Mzerd A., Taibi M., Ouhimmou. S. and Benbihm H. (2019): *Mathematical and numerical modeling of energy recovery of sunflower waste.*– (IREA), vol.7, No.5. pp.160-177.

[16] Obeidi M.A., Healy P. and Alobaidi H. (2024): *Towards a sustainable laser powder bed fusion process via the characterisation of additively manufactured nitinol parts.*– Mechanical Engineering Design, vol.8, No.3, p.45, https://doi.org/10.3390/designs8030045.

[17] Kurian A., Arivazhagan N. and Senthilkumaran K. (2014): *Numerical and experimental investigations on laser melting of stainless steel 316L metal powders.*– Journal of Manufacturing Processes, vol.16, No.3, pp.345-355.

[18] Yadroitsev I., Gusarov A.V., Yadroitsava I. and Smurov I. (2010): *Single track formation in selective laser melting of metal powders.*– Journal of Materials Processing Technology, vol.210, No.12, pp.1624-1631.

[19] Kokare S., Oliveira J.P. and Godina R. (2023): *A LCA and LCC analysis of pure subtractive manufacturing, wire arc additive manufacturing, and selective laser melting approaches.*– J. Manuf. Process., vol.101, pp.67-85.